RSC Advances

PAPER

View Article Online
View Journal | View Issue

Check for updates

Cite this: *RSC Adv.*, 2019, **9**, 21947

Received 5th March 2019
Accepted 5th July 2019

DOI: 10.1039/c9ra01675a

rsc.li/rsc-advances

Morphology control of α-Fe_2O_3 towards super electrochemistry performance

Ruili Zhang, Debao Liu and Ping Yang *

α-Fe_2O_3 with various morphologies including spindle, rod, tube, disk, and ring were synthesized through controlling the $H_2PO_4^-$ etching process. The concentrations of $H_2PO_4^-$ plays an important role in controlling the morphology change of the samples. Selected adsorption of $H_2PO_4^-$ ions resulted in anisotropic growth. In addition, the etching of $H_2PO_4^-$ occurred in the center of rods which resulted in tubal α-Fe_2O_3. Nanodiscs were created once the etching process occurred on the wall of the tube. The electrochemical test shows that disklike samples revealed excellent specific capacitance, rate capacity and cycling stability because of relative higher surface area and pore structure. For the CO catalytic oxidation properties, spindle samples exhibited super catalytic activity.

Introduction

It is well known that the properties of nanomaterials depend not only on the chemical composition and crystal structure, but also on the morphology, size and exposed facets. Unique structures and morphologies of nanomaterials reveal technological significance in energy storage and conversion as well as catalysis. The synthesis of these nanomaterials was carried out by controlling the preparation process.[1,2] Because the nucleation and growth of materials are very sensitive, the morphology of the resulting samples was controlled by the anisotropy of crystal. In particular, nanostructures with different dimensions (0 to 3D) are synthesized through the selective adsorption of ligand ions.[3–5] Thus, the control of the synthesis process *via* special methods (*e.g.* ion etching) is crucial for creating nanomaterials with special structures.

Hematite α-Fe_2O_3, as an n-type semiconductor ($E_g = 2.1$ eV), is the most stable structure iron oxide at ambient conditions.[6] Benefiting from some merits, such as low cost, environmentally friendly, nontoxic, corrosion resistant and easily obtainable, the hematite has been widely used in the fields of catalysts, energy conversion and sensors.[7–9] So far, the α-Fe_2O_3 with different morphologies including sphere, rod, wire, spindle, nut, rice and mesoporous structure have already been fabricated by a variety of processes.[10–16] For example, hollow structures are obtained by controlled deposition of the precursors onto diverse removable templates *via* chemical etching or thermal decomposition. Namely, the synthesis methods generally contain sol–gel processing, micro-emulsion, chemical precipitation and hydrothermal method.[17–20] Among these methods, a hydrothermal method offers effective control over the nucleation and growth by controlling the experimental parameters. Moreover, the obtained products usually present good dispersion, uniformity without agglomeration and high purity.[21] In fact, the simple synthesis strategy without templates for hollow α-Fe_2O_3 hierarchical structures is still remains a technological challenge in spite of extensive research efforts.

In this paper, $H_2PO_4^-$ ions driven etching process was developed to fabricate α-Fe_2O_3 nanostructures with a series of morphologies including spindle, tube, disk and ring without using templates. The amount of $H_2PO_4^-$ ions controlled the etching process which determined the morphology of resulting samples. The morphologies and structures of resulting samples were fully investigated and the oriented dissolution and recrystallization formation mechanism was proposed by changing preparation parameters. In addition, the supercapacitor and catalytic measurements were performed towards electrochemical performance and CO catalytic oxidation properties.

Experimental

Synthesis of samples

Chemicals were of analytical grade and used as received without further purification. In a typical synthesis, 0.1162 g of $FeCl_3\cdot 6H_2O$ was dissolved in 30 mL of distilled water with stirring for 30 min. Different amount of $NaH_2PO_4\cdot 2H_2O$ (0, 0.21, 0.43, 0.64, 1.0, 2.5, and 3.0 mM) was then added into above yellow aqueous solutions with stirring for 30 min and after that transferred into a Teflon-lined stainless steel autoclave. The autoclave was sealed and maintained at 220 °C for 3–20 h. Finally, the autoclave was cooled to room temperature naturally. Samples were separated by centrifugation and washed with water for 3 times and dried at 70 °C in air. The preparation conditions and morphologies are listed in Table 1.

School of Material Science and Engineering, University of Jinan, Jinan, 250022, P. R. China. E-mail: mse_yangp@ujn.edu.cn

Table 1 Preparation conditions and morphology of samples[a]

Sample	$H_2PO_4^-$ (mM)	Molar ratio[b]	Time (h)	Morphology
S1	N/A	N/A	20	Quasi-sphere
S2	0.21	71	20	Spindle
S3	0.43	35	20	Rod
S4	0.64	23	20	Tube
S5	1	15	20	Disk
S6	2.5	6	20	Ring
S7	3	5	3	Disk
S8	3	5	6	Hole in center
S9	3	5	12	Ring
S10	3	5	20	Ring

[a] The concentration of Fe^{3+} was 15 mM for all samples. [b] The molar ratio of $Fe^{3+}/H_2PO_4^-$.

Characterization

The morphology and microstructure observation of samples were carried out using field-emission scanning electron microscopy (SEM, QUANTA 250 FEG, FEI, America) and high-resolution transmission electron microscopy (HRTEM, JEOL JEM-2100). The crystal structures and phase composition of samples were taken on an X-ray diffraction (XRD) meter (Bruker, D8 ADVANCE) with Cu K_α irradiation (k = 1.5406 Å). The specific surface areas of samples were characterized by nitrogen adsorption–desorption measurement (MFA-140, Beijing Builder Company). A high-resolution Raman spectrometer (LabRAM HR Evolution, HORIBA JOBIN YVON SAS) was used to record the Raman spectra of samples. The Fourier-transform infrared spectroscopy (FI-IR) spectra of samples were recorded on a WQF-410 spectrophotometer (Beijing Secondary Optical Instruments, China).

Electrochemical measurement

A working electrode was prepared by mixing active material, acetylene black, and polyvinylidene fluoride (PVDF) in a mass ratio of 80 : 15 : 5 and stirred for 1 h to form homogeneous slurry. The slurry was subsequently brush-coated on a nickel foam and dried at 70 °C overnight to evaporate the solvent. An individual electrode contained active material of about 3.0 mg and a working electrode was obtained by pressing an active material-coated Ni foam at 10 MPa. A three-electrode electrochemical system was used to measure the electrochemical behavior of the samples, where the active material, Pt foil and Hg/HgO electrode were employed as working electrode, counter electrode and reference electrode, respectively. The cyclic voltammetry (CV) and galvanostatic charge–discharge (GCD) measurements were performed using an electrochemical work station (CHI 660E, Chenhua, Shanghai) in a 6 M KOH aqueous solution. The electrochemical impedance spectroscopy (EIS) measurement was carried out by applying an AC amplitude of 5 mV at open circuit potential. The specific capacitance was calculated from the GCD curves using the following equation:

$$C = (I \times \Delta t)/(m \times \Delta V)$$

where, I is applied current (A), Δt is discharge time (s), ΔV (v) is sweep potential window and m (g) is the mass of the active materials.

Catalytic measurement

CO oxidation activity was measured in a fixed-bed flow reactor (outer diameter of 6 nm) at the atmospheric pressure and with 50 mg of catalyst. The reactants were fed with a volume ratio of $He/CO/O_2 = 79/1/20$ (a total flow rate of 30 mL min^{-1}) controlled by independent thermal mass flow controllers. The effluent gases were analyzed online using a gas chromatograph equipped with a flame ionization detector. The CO conversion ratio of samples was calculated using an equation bellow.

$$\text{CO conversion} = [(\text{CO}_{\text{in}} - \text{CO}_{\text{out}})/\text{CO}_{\text{in}}] \times 100\%$$

where, CO_{in} and CO_{out} are inlet and outlet CO concentration, respectively.

Results and discussion

Morphology evolution mechanism, crystal structure and phase composition of samples

Fig. 1 shows the SEM images of samples S1 to S6. For sample S1 (no $H_2PO_4^-$ addition), quasi spheres with a relatively small diameter of 60–90 nm were observed as shown in Fig. 1a. This is related to isotropic growth. Sample S2 prepared with a low $H_2PO_4^-$ concentration revealed a spindle morphology with a length of 200–267 nm and average diameter of 45 nm as shown in Fig. 1b. The inset in Fig. 1 shows the HRTEM image of a particle which confirms the growth is along [001] direction (c axis). Similar phenomenon was observed in literature.[13,15] This confirms the adsorption ability of $H_2PO_4^-$ ions on the (001) facet was low compared with other planes, the (001) plane was less protected. With further increasing $H_2PO_4^-$ concentration to 0.43 mM, sample S3 exhibited rod morphology with a length of 150–176 nm and average diameter of 70 nm (Fig. 1c, S3). The tube morphology was observed on the top of the specimen as circled in some area in Fig. 1c. This means large amount $H_2PO_4^-$ ions limited the growth of samples. The change of morphology and size confirms that $H_2PO_4^-$ ions plays an important role.

Compared with samples S2 and S3, the rod morphology is seemingly obtained by cutting the tips of spindle. This confirms the etching occurred because of the reaction of excess $H_2PO_4^-$ ions with Fe_2O_3. This is ascribed to the dissolution of spindles along the long axis direction. Similar phenomenon was observed in literature.[13] In addition, the diameter of samples increased with increasing $H_2PO_4^-$ concentrations. This is ascribed the re-growth of Fe_2O_3 on diameter direction because of Fe precursors generated by the etching. With increasing the concentrations of $H_2PO_4^-$ ions to 0.64 mM, the resulting sample become into tube-like morphology with average length of 160 nm and diameter of 100 nm (Fig. 1d, sample S4). For a $H_2PO_4^-$ concentration of 1 mM, the product was identified as disk-like shape with an average size of 126 nm (Fig. 1e, sample S5). In the case of $H_2PO_4^-$ concentration of 2.5 mM, the product was changed into ring-like

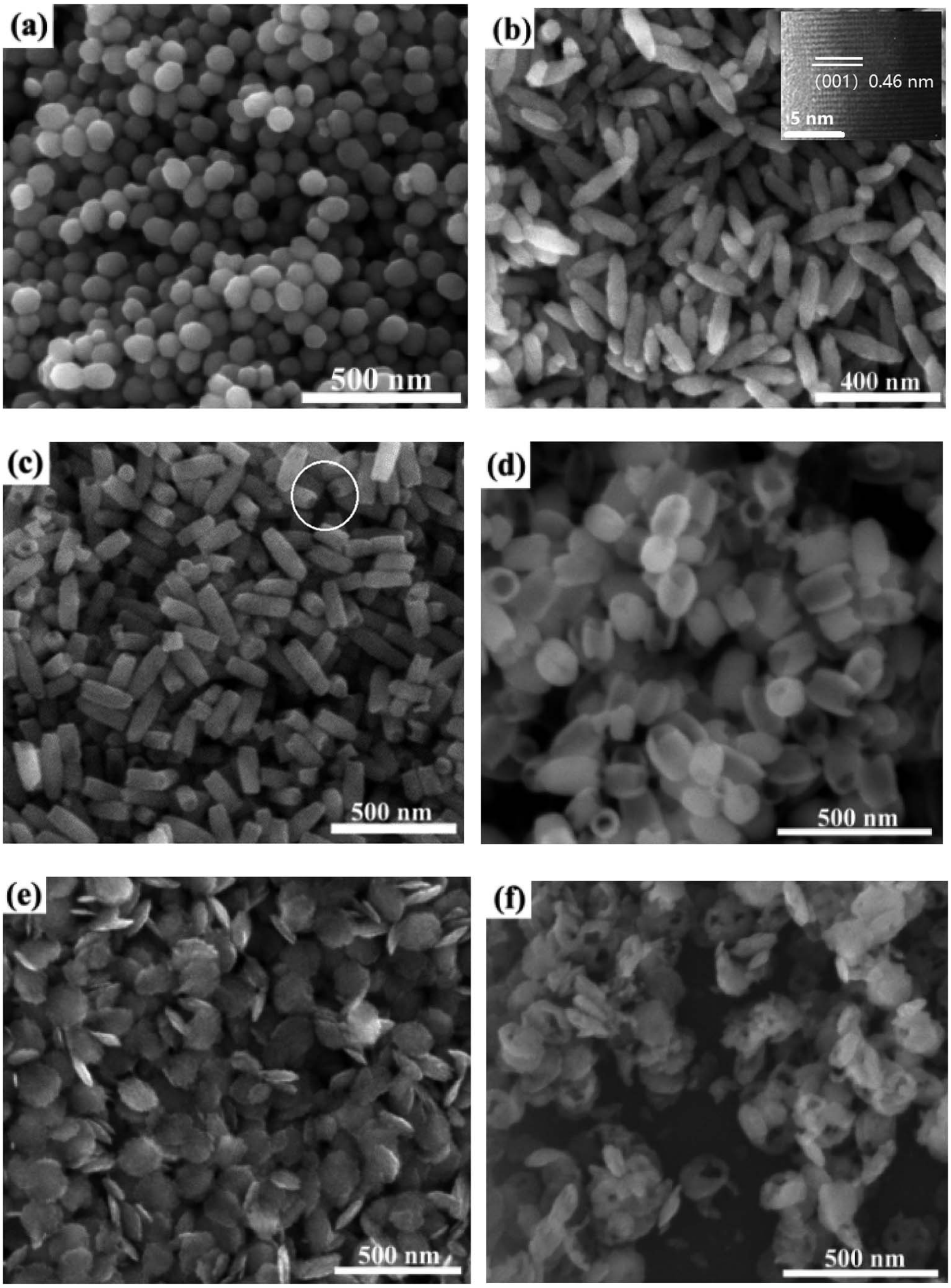

Fig. 1 SEM images of samples. (a) S1, (b) S2, (c) S3, (d) S4, (e) S5, and (f) S6. The inset in (b) shows the TEM image of a α-Fe_2O_3 particle (S2). The lattice fringes in the inset show the growth along (001) facet.

structures with outer diameter of 130 to 160 nm and the thickness of the wall was about 40–60 nm (Fig. 1f, sample S6).

According to the morphology evolution in Fig. 1, it is found that $H_2PO_4^-$ concentrations play an important role for the resulting shape of samples. Similar phenomenon was observed by Chen *et al.*[22] The morphology evolution mechanism is schematized in Fig. 2. Without $H_2PO_4^-$, quasi spheres were obtained because of isotropic growth. With increasing the concentration of $H_2PO_4^-$ ions, the selected adsorption of $H_2PO_4^-$ ions occurred on the different facets of Fe_2O_3 samples. The adsorption of $H_2PO_4^-$ ions is very weak for the (001) plane because of the lack of singly coordinated hydroxyl groups.[22,24] Thus $H_2PO_4^-$ ions were located on the prism planes of (110) and (100). The growth occurred along [001] direction, which resulted in the formation of spindle like Fe_2O_3 particles. As the $H_2PO_4^-$ concentration continues increasing, the tips of spindle-shaped particles were concaved to form nanorods. The driving force is the high activity of the sharp spindle tips, which are easily attacked by the protons in acidic solution. With the $H_2PO_4^-$ concentration further increasing, nanotubes were obtained.

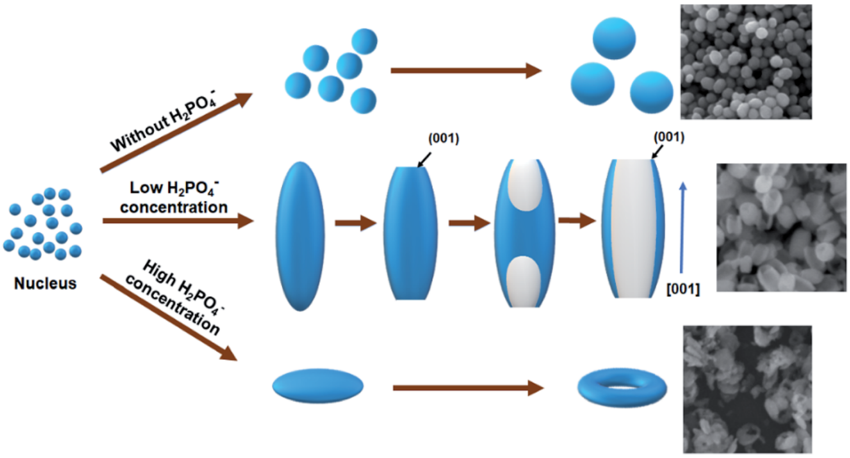

Fig. 2 Morphology evolution process of samples.

The formation of nanotubes can be described as dissolution of the spindle-shaped precursors from the tips toward the interior along the long axis, finally hollow tubes are formed. When the concentration of $H_2PO_4^-$ was high (1 mM), a large amount of surface adsorbed $H_2PO_4^-$ made the nanoparticles surface more negatively charged. Therefore, the electrostatic repulsion made aggregation of the nanoparticles difficult. Instead of forming spindle-shaped particles, nanodiscs were obtained.[22] Similar to the nanotubes in the solution with a low phosphate concentration, the central area on both faces of a nanodisc was dissolved throughout the whole particle, a hole was made along the [001] direction and a nanoring appeared.[22–24]

To confirm the phase composition, Fig. 3 shows the XRD patterns of samples with different concentrations of $H_2PO_4^-$. It is found that samples S1–S4 revealed pure α-Fe_2O_3 phase (all diffraction peaks matched perfectly with JCPDS file no 33-0664) without any other impurities. Moreover, all the diffraction peaks in XRD patterns are narrow and sharp, indicating ideal crystallinity. However, for the samples S5 and S6, apart from a pure α-Fe_2O_3 phase, the XRD peaks of $Fe_4(PO_4)_3(OH)_3$ (JCPDS file no 42-0429) phase were observed. Especially for sample S6, the XRD peaks of $Fe_4(PO_4)_3(OH)_3$ phase became high. This is ascribed to the reaction of $H_2PO_4^-$ ions with Fe_2O_3.[25]

To confirm the role of $H_2PO_4^-$ role, the FT-IR spectra of samples with different morphologies are shown in Fig. 4a. A distinct peak at 3450 cm^{-1} is ascribed to the bending frequency of surface hydroxyl group,[26] and the strong absorption band centred at 573 cm^{-1} is due to the Fe–O vibrational mode, which is the typical lattice vibration peak of α-Fe_2O_3.[27,28] Some weak peaks between 1010 and 1022 cm^{-1} confirm the presence of some phosphate impurity in samples.[29] Fig. 4b depicts the Raman spectra of samples. Clearly, the Raman vibration bands at 228.31, 290.45, 410.48, 505.94, 656.11 and 1315.84 cm^{-1} indicated the formation of α-Fe_2O_3. The peaks at 228.31 and 505.94 cm^{-1} represented the typical A 1g mode, while the peaks at 290.45, 410.48, 656.11 and 1315.84 cm^{-1} are due to the E_g mode.[30]

According to the result in literature, the surface hydroxyl configuration on (001) planes of α-Fe_2O_3 was doubly coordinated hydroxyl groups, whereas on other planes, for instance the (012), (110) and (100) plane, the dominated surface coordinated hydroxyl groups are singly type.[31–34] The $H_2PO_4^-$ in solution can react with hydroxyl groups by forming monodentate or bidentate inner-sphere complex.[35,36] Thus, the adsorption capacities and affinities for phosphate to hematite were much lower for the (001) planes than for the others.

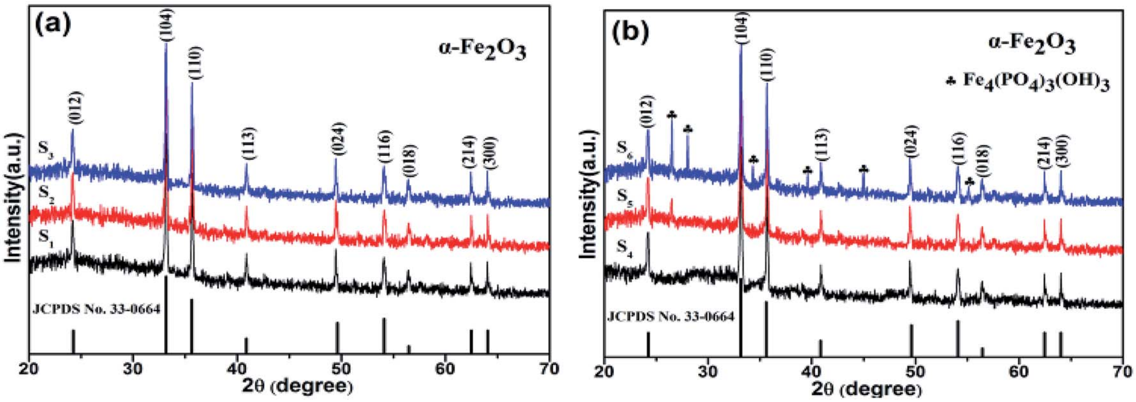

Fig. 3 XRD patterns of samples with different $H_2PO_4^-$ concentrations.

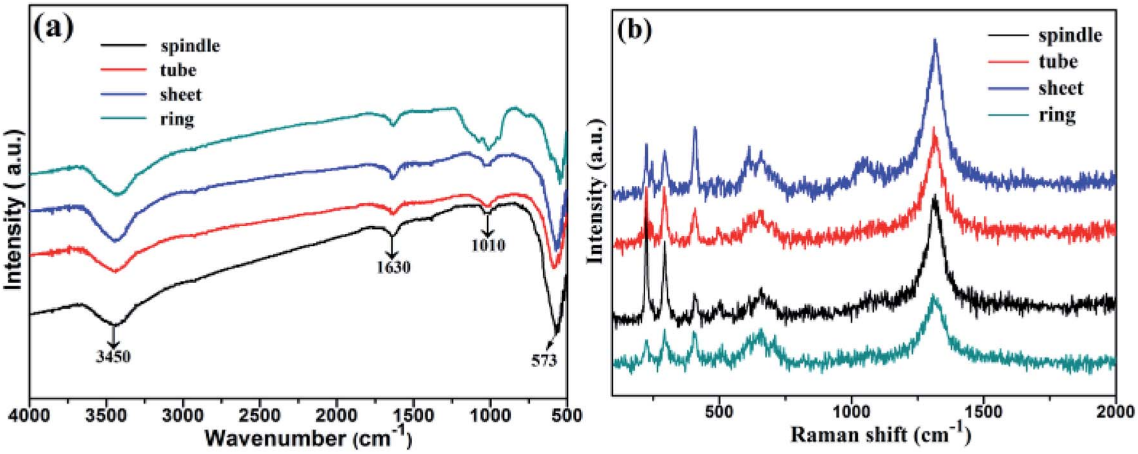

Fig. 4 (a) FT-IR spectra and (b) Raman spectra of samples.

At low $H_2PO_4^-$ concentration, selected adsorption occurred on the planes except for (001) plane due to the special surface hydroxyl configuration. Thus, the (001) plane would grow quick compared with others and result in spindle-like structure based on the theory that the final morphology is determined by those planes with low growth speed.

$$Fe_2O_3 + 2xH_2PO_4^- + 6H^+ \leftrightarrow 2[Fe(H_2PO_4)_x]^{3-x} + 3H_2O \quad (1)$$

With increasing $H_2PO_4^-$ concentration to 0.43 mM, the spindle-like products would form at first. At the same time, the H^+ concentration would increase due to the continuous hydrolysis of Fe^{3+}, which accelerates eqn (1) towards the positive direction. Therefore, the etching process would happen along [001] direction because of high activity of the sharp spindle tips and formed the final rod-like shape at the state of solution system equilibrium. For $0.64H_2PO_4^-$ concentration, the morphology evolution is as same as the formation of rod-like product. The center area was completely dissolved and the diameter of the final tube became larger and the surface smoother than that of the spindle-like products. At a high $H_2PO_4^-$ concentration (1 mM), the resulting samples exhibited a disk-like morphology with the main exposed (001) plane. This is ascribed that the surface hydroxyl groups were intense protonized because of a high $H_2PO_4^-$ concentration and more $H_2PO_4^-$ ions adsorbed on the (001) plane with less Fe^{3+} adsorbed due to the electrostatic attraction.[37] As a result, the growth of (001) plane was blocked and became a final main exposed plane.

The SEM images of samples are shown in Fig. 5. In addition, a time-dependent morphology evolution test and the corresponding formation mechanism was also given in Fig. 6. With a constant $H_2PO_4^-$ concentration, it is found that the samples underwent shape evolution with various time. When the reaction time was 3 h, the products present disk-like morphology with diameter of about 140 nm (Fig. 5a, sample S7). Prolonging the reaction time to 6 h, the center of some disks became thinner and small holes were observed in the center and the diameter increased to about 145 nm (Fig. 5b, sample S8). With further prolonging time to 12 h, thinner areas increased in the center of disks and the holes became large and some disks are penetrated obviously with an average diameter of 157 nm (Fig. 5c, sample S9). When the reaction time reached to 20 h, the holes became large and most of the products became into ring-like morphology. The outer diameter increased to about 166 nm (Fig. 5d, sample S10). Apparently, the outer diameter of sample S10 increased with about 26 nm compared with sample S7.

Fig. 6 shows the formation scheme of ring structure. The dissolving process along the [001] direction of the disks results to the formation of the ring. Since different planes share different surface hydroxyl configuration and the reaction on (001) plane was accelerated to the right side of eqn (1) and the α-Fe_2O_3 was dissolved faster than that of other planes. So the concentration of $[Fe(H_2PO_4)_x]^{3-x}$ in the solution was enhanced and the $H_2PO_4^-$ decreased. According to the equilibrium theories,[38] the (012) facet can absorb the new produced $[Fe(H_2PO_4)_x]^{3-x}$ and release new $H_2PO_4^-$ to keep balance of the solution system. Hence, the (012) plane grew naturally which gives a good explanation of the increased diameter in ring-like products.

Electrochemical properties

The electrochemical measurements of samples were characterized in a three-electrode configuration with 6 M KOH electrolyte. The CV curves of sample S5 electrode with different scan rate are shown in Fig. 7a. It is found that the peak current depends linearly on the sweep rate and a pair of redox peaks present at each curve, which is the features of Faraday redox reaction. The peaks retain well at high scanning rates, indicating the fast electronic and ionic transport process. Moreover, due to the interface resistance of the electrode, the anodic peak moves toward more anodic and the cathode peak moves toward more cathode with the increasing scan rates. Fig. 7b depicts the charge–discharge curves of the electrodes with various current densities. The specific capacitance values are 362, 345, 330, 310 and 272 F g^{-1} at different current densities of 0.5, 1, 2, 3 and 5 A g^{-1}, respectively. Fig. 7c is the charge–discharge curves (at 1 A g^{-1}) of the four samples with various morphologies. Clearly, the S5 (disk-like) sample possess highest discharge times, indicating the best specific capacitance. From the Table 2, we

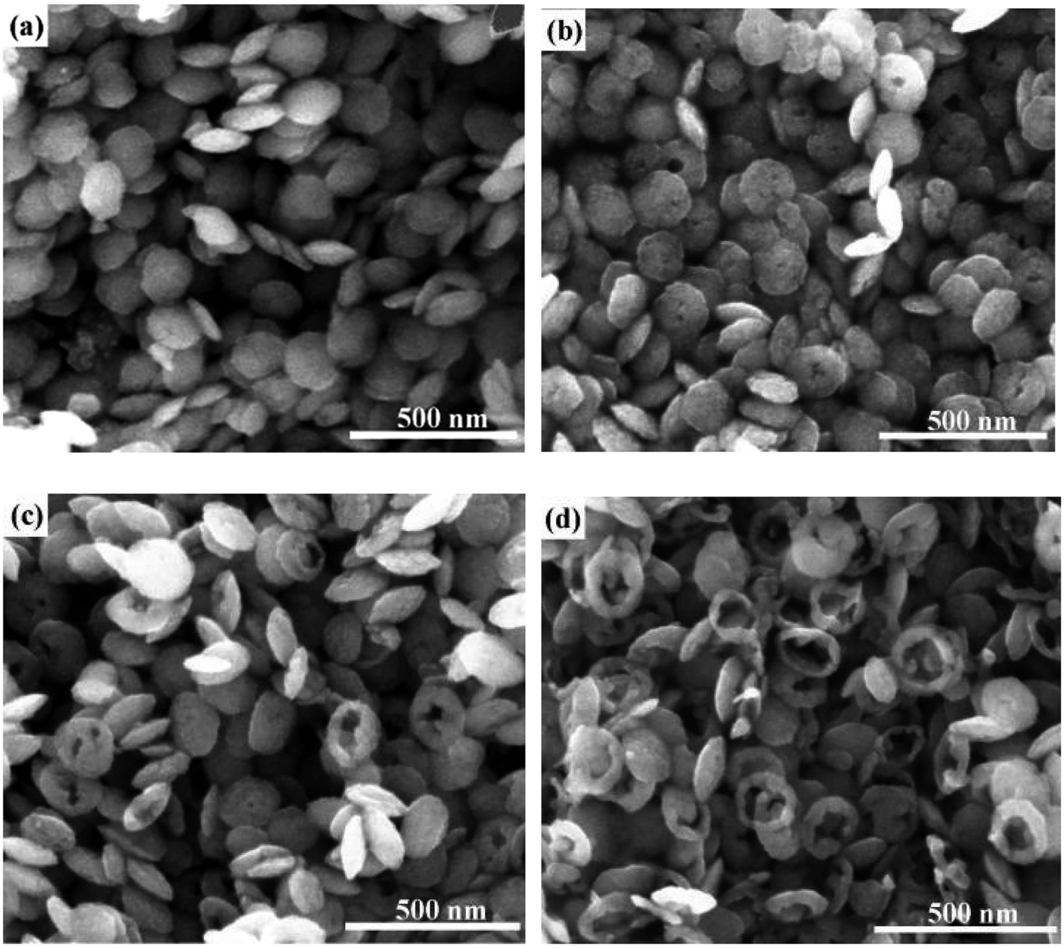

Fig. 5 Morphology evolution of samples with different reaction time. (a) S7, (b) S8, (c) S9, (d) S10.

can see that the specific capacitance values of the four samples follows the order: spindle < tube < ring < disk.

The variation trend of specific capacitance as a function of current density for the samples is shown in Fig. 7d. At a current density of 10 A g^{-1}, the specific capacitance of sample S5 (disk-like) electrode can also maintain as high as 260 F g^{-1} with 69.3% retention, which indicates that the disk-like structure is more beneficial to the enhancement of rate capacity. On the contrary, the sample S2 (spindle-like) sample exhibits inferior specific capacitance and poor rate capability. Except for the electrochemical behavior and capacitance properties of the products, a good cycling stability is of great importance. So we tested the cycling performance of sample S5.

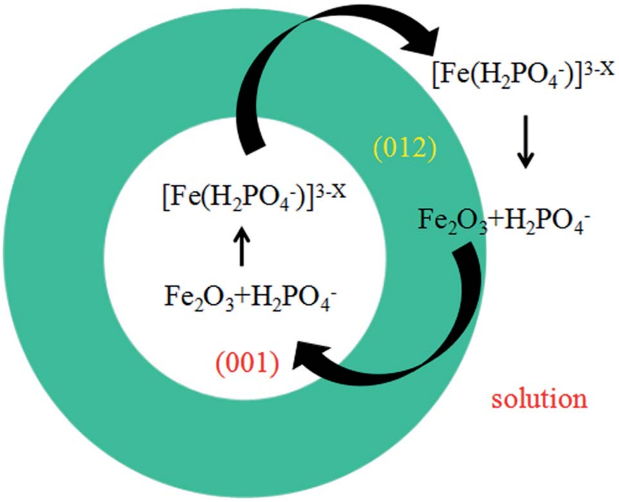

Fig. 6 Schematic illustration for formation of ring-like structure.

Fig. 7e is the specific capacitance retention of sample S5 at a current density of 5 A g^{-1} after 5000 cycles. In the first 200 cycles, the as-prepared electrode exhibits a stable capacitance with nearly unchanged, in the following cycling process, the electrode also exhibits ideal specific capacitance with a retention about 70.5%, which indicating that the disk-like structures present an excellent cyclability. Also, the curves of charge–discharge time are almost unchanged for the first 10 cycles, indicating high coulombic efficiency. Fig. 7f represents the EIS measurements of samples with various morphologies. The Nyquist plots contain two parts: the semicircle at high frequency region and the curve at low frequency region. While the intersection of the semicircle and real axes represents ohm resistance (R_s), including the intrinsic resistance of the substrate.[39] The diameter of the semicircle indicates the interface charge transfer resistance between the electrode and the

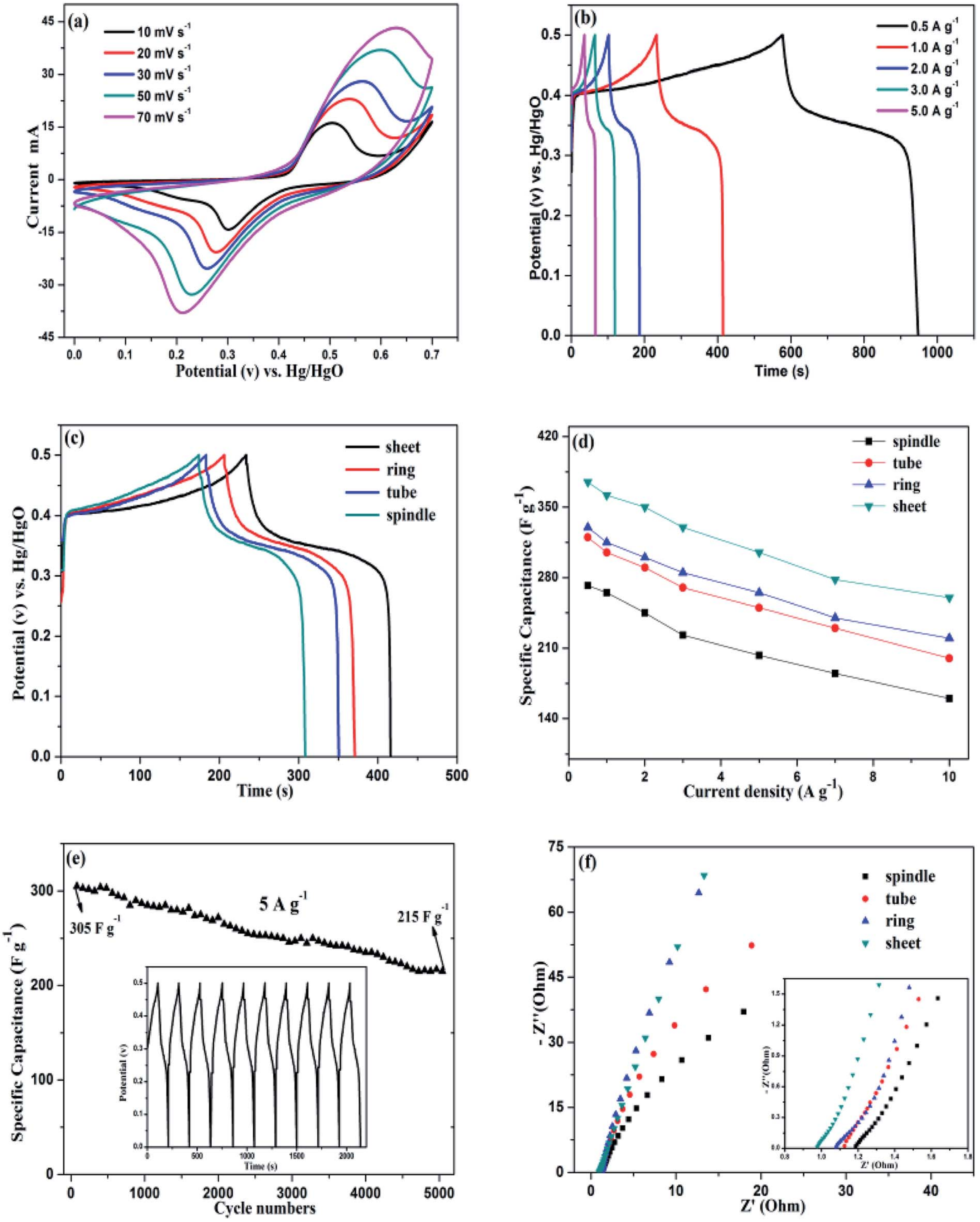

Fig. 7 (a) Cyclic voltammetry curves at different scan rates and (b) charge–discharge curves at various current densities of sample S5. (c) Charge–discharge curves of four samples with various morphologies at a current density of 1 A g^{-1}. (d) The specific capacitances of the four electrode materials at different current densities. (e) Cycle performance of sample S5 at a current density of 5 A g^{-1}; (f) the Nyquist plots of samples with different morphologies.

electrolyte (R_{ct}). The R_s values of the electrodes can be clearly seen from the illustration and follows the order: disk < ring < tube < spindle, demonstrating the best electrical conductivity for disk-like sample. The results consist with the previous analysis of the charge–discharge curves. The slope of the curve at low frequency region represents the diffusion resistance of

Table 2 Specific capacitance of samples[a]

Samples	Specific capacitance (F g^{-1})
S2	272
S4	310
S5	360
S6	330

[a] At a current density of 1 A g^{-1}.

OH^- ions (Warburg resistance).[40] It is found that the sample S5 performs highest slope value and more closer to the virtual axis, indicating smallest diffusion resistance. The reasons can be ascribed to the unique disk-like structure: the large specific surface area and considerable open space caused by the porous structure, demonstrating an ideal electrode material for charge migration and ion diffusion.

CO catalytic oxidation properties

The CO catalytic oxidation properties of four samples with different morphologies were characterized. Seen from Fig. 8, due to the continuous oxidation of CO, the CO conversion ratios were gradually increased with temperature. Obviously, the sample S2 (spindle-like) structure of α-Fe_2O_3 performs the best catalytic property: the onset oxidation temperature (T_{10}) and the completed CO oxidation temperature (T_{100}) were 268 and 300 °C, respectively. The key factor that determines the catalytic performance lies in the exposed specific crystal facets of the samples. And the Fe atoms on the crystal plane are the catalytic active center. Therefore, the higher the Fe atoms density, the better the catalytic performance. According to the result in literature,[41,42] the main exposed surface of the sample S2 (spindle-like) samples is (012) plane and the corresponding Fe atoms density is about 10.1 atoms per nm^2, which could provide more active sites for catalytic reactions and have the highest catalytic activities. Therefore, the order of the catalytic activity of the four samples is tube-like < disk-like < ring-like < spindle-like.

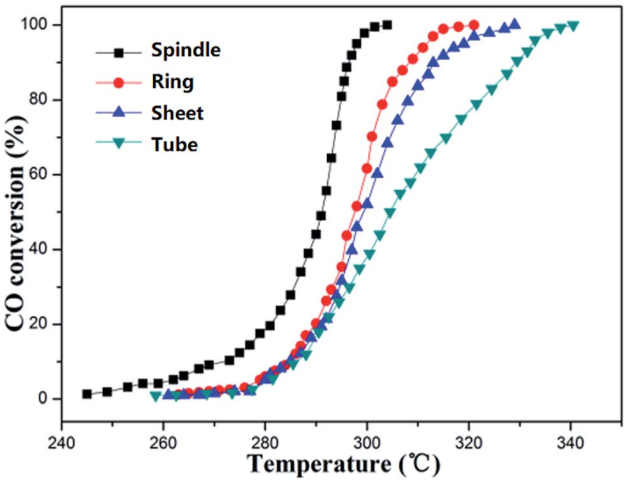

Fig. 8 CO oxidation of samples as a function of reaction temperature.

Conclusions

In summary, a series of different morphologies of α-Fe_2O_3 were synthesized under the control of $H_2PO_4^-$ ions. It was found that the $H_2PO_4^-$ concentration has an important influence on the morphologies of the products. The final morphologies of the products mainly depend on the growth control of $H_2PO_4^-$ to the unique (001) plane. The electrochemical measurements show that the samples with various morphologies exhibit different specific capacities and the disk-like products exhibit excellent specific capacitance and ideal cycling stability due to the relative higher specific surface area and opened pore structure. For the CO catalytic oxidation properties, the specific exposed facets on α-Fe_2O_3 are indeed factors influencing the catalytic performances. In addition, the spindle-like α-Fe_2O_3 performs the best catalytic property. The reason is that the main exposed facets is the (012) plane which has a larger Fe atom density and provides more catalytic active sites. As a result, the spindle-like α-Fe_2O_3 demonstrating excellent catalytic performance.

Conflicts of interest

There are no conflicts to declare.

Acknowledgements

This work was supported by the projects from National Natural Science Foundation of China (grant nos. 51572109 and 51772130).

References

1 A. Seyed-Razavi, I. K. Snook and A. S. Barnard, *J. Mater. Chem.*, 2010, **20**, 416–421.
2 M. V. Kovalenko, M. I. Bodnarchuk, R. T. Lechner, G. Hesser, F. R. Schaffler and W. G. Heiss, *J. Am. Chem. Soc.*, 2007, **129**, 6352–6353.
3 J. J. Li, P. Jia, X. Hu, D. H. Dong, G. G. Gao, D. S. Geng, J. Xiang, Y. Wang and S. Hu, *Mol. Catal.*, 2018, **450**, 1–13.
4 L. B. Yu, J. J. Wang, X. Hu, Z. M. Ye, C. Buckley and D. H. Dong, *Electrochem. Commun.*, 2018, **86**, 72.
5 L. L. Wang, T. Fei, Z. Lou and T. Zhang, *ACS Appl. Mater. Interfaces*, 2011, **3**, 4689–4694.
6 H. B. Guo and A. S. Barnard, *J. Mater. Chem. A*, 2013, **1**, 27–42.
7 S. Y. Lian, E. B. Wang, L. Gao, D. Wu, Y. L. Song and L. Xu, *Mater. Res. Bull.*, 2006, **41**, 1192–1198.
8 H. W. Wang, Z. J. Xu, H. Yi, H. G. Wei, Z. H. Guo and X. F. Wang, *Nano Energy*, 2014, **7**, 86–96.
9 J. Chen, L. N. Xu, W. Y. Li and X. L. Gou, *Adv. Mater.*, 2005, **17**, 582–586.
10 Q. Liu, Z. M. Cui, Z. Z. Ma, S. W. Bian, W. G. Song and L. J. Wan, *Nanotechnology*, 2007, **18**, 385605.
11 K. Woo, H. J. Lee, J. P. Ahn and Y. S. Park, *Adv. Mater.*, 2003, **15**, 1761–1764.
12 Q. Han, Z. H. Liu, Y. Y. Xu, Z. Y. Chen, T. M. Wang and H. Zhang, *J. Phys. Chem. C*, 2007, **111**, 5034–5038.

13 X. Li, X. Yu, J. H. He and Z. Xu, *J. Phys. Chem. C*, 2009, **113**, 2837–2845.
14 S. H. Lee and C. M. Liddell, *Small*, 2009, **5**, 1957–1962.
15 H. Wang, D. W. Brandl, F. Le, P. Nordlander and N. J. Halas, *Nano Lett.*, 2006, **6**, 827–832.
16 F. Jiao, A. Harrison, J. C. Jumas, A. V. Chadwick, W. Kockelmann and P. G. Bruce, *J. Am. Chem. Soc.*, 2006, **128**, 5468–5474.
17 X. Q. Liu, S. W. Tao and Y. S. Shen, *Sens. Actuators, B*, 1997, **40**, 161–165.
18 I. Ray, S. Chakraborty, A. Chowdhury, S. Majumdar, A. Prakash, R. Pyare and A. Sen, *Sens. Actuators, B*, 2008, **130**, 882–888.
19 D. Yener and H. Giesche, *J. Am. Ceram. Soc.*, 2001, **84**, 1987–1995.
20 R. D. Zysler, M. Vasquez-Mansilla, C. Arciprete, M. Dimitrijewits, D. Rodriguez-Sierra and C. Saragovi, *J. Magn. Magn. Mater.*, 2001, **224**, 39–48.
21 X. Liu, G. Qiu, A. Yan, Z. Wang and X. Li, *J. Alloys Compd.*, 2007, **433**, 216–220.
22 J. Chen, S. Macfarlane, C. Zhang, K. Yu and W. Zhou, *Cryst. Growth Des.*, 2017, **17**, 5975–5983.
23 X. Yan, Y. Wu, D. Li, C. Luo, Y. Wang, J. Hu, G. Li, P. Li, H. Jiang and W. Zhang, *J. Mater. Sci.: Mater. Electron.*, 2018, **29**, 2610–2617.
24 C. Jia, L. Sun, F. Luo, X. Han, L. J. Heyderman, Z. Yan, C. Yan, K. Zheng, Z. Zhang, M. Takano, N. Hayashi, M. Eltschka, M. Kläui, U. Rüdiger, T. Kasama, L. Cervera-Gontard, R. E. Dunin-Borkowski, G. Tzvetkov and J. Raabe, *J. Am. Chem. Soc.*, 2008, **130**, 16968–16977.
25 K. Byrappa and T. Adschiri, *Prog. Cryst. Growth Charact. Mater.*, 2007, **53**, 117–166.
26 C. T. Liu, J. Ma and Y. L. Liu, *Sci. China: Chem.*, 2011, **54**, 1607–1614.
27 L. Li and K. Y. S, *Chem. Res. Chin. Univ.*, 2009, **25**, 595–599.
28 Q. Song and Z. J. Zhang, *J. Am. Chem. Soc.*, 2004, **126**, 6164–6168.
29 G. K. Pradhan and K. M. Parida, *ACS Appl. Mater. Interfaces*, 2011, **3**, 317–323.
30 Z. J. Zhang, X. J. Mei, L. R. Fen, S. J. Lu and F. L. Qiu, *Chin. Chem. Lett.*, 2004, **15**, 867–870.
31 G. K. Pradhan, D. K. Padhi and K. M. Parida, *ACS Appl. Mater. Interfaces*, 2013, **5**, 9101–9110.
32 X. L. Hu and J. C. Yu, *Adv. Funct. Mater.*, 2011, **13**, 7293–7298.
33 B. L. Lv, Y. Xu, D. Wu and Y. H. Sun, *J. Nanosci. Nanotechnol.*, 2010, **10**, 2348–2359.
34 J. D. Russell, R. L. Parfitt, A. R. Fraser and V. C. Farmer, *Nature*, 1974, **248**, 220–221.
35 J. Zhao, P. Yang, H.-S. Chen, J. Li, Q. Che, Y. Zhu and R. Shi, *J. Mater. Chem. C*, 2015, **3**, 2539–2547.
36 V. Barrón and J. Torrent, *J. Colloid Interface Sci.*, 1996, **177**, 407–410.
37 X. Huang, *J. Colloid Interface Sci.*, 2004, **271**, 296–307.
38 X. L. Hu, J. C. Yu, J. M. Gong, Q. Li and G. S. Li, *Adv. Mater.*, 2007, **19**, 2324–2329.
39 C. J. Jia, L. D. Sun, Z. G. Yan, L. P. You, F. Luo, X. D. Han, Y. C. Pang, Z. Zhang and C. H. Yan, *Angew. Chem.*, 2005, **117**, 4402–4407.
40 G. Binitha, M. S. Soumya, A. A. Maahavan, P. Praveen, A. Balakrishnan, K. R. V. Subramanian, M. V. Reddy, V. Shantikumar, A. Nair, S. Nair and N. Sivakumar, *J. Mater. Chem. A*, 2013, **1**, 11698–11704.
41 R. Khan, M. Habib, M. A. Gondal, A. Khalil, Z. U. Rehman, Z. Muhammad, Y. A. Haleem, C. D. Wang, C. Q. Wu and L. Song, *Mater. Res. Express*, 2017, **4**, 105501–105510.
42 Q. X. Gao, X. F. Wang, J. L. Di, X. C. Wu and Y. R. Tao, *Catal. Sci. Technol.*, 2011, **1**, 574–577.